

Low-Order Prediction of Wing Wakes in the Vicinity of Tail Surfaces

Pranav Hosangadi* and Ashok Gopalarathnam†

*Department of Mechanical and Aerospace Engineering,
North Carolina State University, Raleigh, NC 27695-7910*

It is well known that inviscid low-order methods such as the vortex lattice method (VLM) can predict the forces and moments on three-dimensional wings of arbitrary plan-form at low angles of attack. This predictive capability can be extended to near-stall and post-stall by modeling the effects of boundary-layer separation as an effective reduction in camber. While wing loads are accurately predicted by such “decambering” methods, the lack of viscous boundary-layer calculations makes them unsuitable for predicting loads on geometries in which the viscous wake from an upstream surface impinges on downstream surfaces. This paper attempts to address this shortcoming by employing semi-empirical equations based on the section drag coefficient to calculate the width of the wake and the velocity profile inside the wake. At every wing section, the velocities induced aft of the wing by the bound and wake vorticity from the low-order decambering method are calculated. The effective trailing-edge height, obtained from the newly introduced nonlinear decambering method, provides a good approximation for the midpoint of the viscous wake at the trailing-edge. A streamline originating at this location, calculated using the induced velocities, gives a good prediction of the centerline of the wake aft of the wing, provided that the midpoint of the wake at the effective trailing edge is correctly identified. This prediction, when used together with the semi-empirical estimates of wake width and velocity deficit, can be useful to calculate wing loads on downstream surfaces in the low-order method.

I. Introduction

Most transport aircraft operate in the “linear regime” of aerodynamics. In this regime, characterized by small angles of attack and largely attached flow, the lift produced varies linearly with angle of attack. The linear regime has been extensively studied and is well understood. Low- α flows can be approximated as inviscid flow with a boundary layer that is small enough to be of little consequence to the lift and moment on the wing. The inviscid flow problem is especially suited to be solved by a low-order method, allowing quick prediction of the forces on the wing for design or simulation purposes. With increasing angle of attack, the adverse pressure gradient on the upper surface of the wing depletes the momentum of the upper-surface flow, causing it to separate. The lift curve is no longer linear, and the actual lift is lower than the lift predicted by an inviscid method. With a further increase in angle of attack, the lift generated peaks and then begins to drop. The angle of attack at which maximum lift occurs is called the stall angle (α_{stall}), and the post-stall regime comes into play at angles higher than α_{stall} . Due to the large influence of the separated boundary layer, such flows can no longer be approximated to inviscid flows and a low-order method must correct for the effects of separation to correctly model the forces and moments in the post-stall regime.

While the post-stall regime has received considerable research attention from the wind turbine and helicopter communities, most of the work done in post-stall aerodynamics with regard to transport aircraft has been in stall prevention and avoidance, since post-stall conditions are only ever experienced by transport aircraft in loss-of-control (LOC) scenarios. Training for recovery from LOC situations is impeded due to the lack of available data for such situations, and an inadequacy of simulator models in accurately replicating

*Graduate Research Assistant, phosang@ncsu.edu. Student Member, AIAA

†Professor, agopalar@ncsu.edu, (919) 515-5669. Associate Fellow, AIAA

post-stall effects. A low-order method capable of accurate post-stall calculations in real time can provide valuable insight into the mechanics of LOC conditions and strategies for recovery, and can be a useful tool in training pilots to handle such situations.

Some research has been carried out to extend low-order models to regimes upto and even slightly beyond stall^{1–14} The decambering approach developed at NCSU^{15, 16} is one such method capable of post-stall predictions by simulating separation using a reduction in the camber of the airfoil at different sections on the wing. The viscous behaviour of the sections is obtained from 2D CFD for unswept wings, and from modification of 2D CFD data for swept wings.¹⁷ The circulation strengths of the vortex lattice elements are calculated ensuring each section is constrained to operate on its viscous lift and moment curves, allowing a low-order method to correctly predict the forces on the wing at stall and beyond. The drawback, however, is that the velocity deficit in the viscous wake cannot be captured because the VLM does not include boundary layer calculations, and hence, the effect of the viscous wake on tail efficiency is not modeled. This paper describes an effort to augment the existing low-order method to predict the extents and velocity deficit in the viscous wake behind a wing near tail surfaces. These predictions can then be used by the low-order method to correctly simulate the loss in tail efficiency and elevator authority in conditions when the tail is within the wake. A newly developed database of RANS CFD simulations¹⁸ is used to validate the predictions of the low-order method.

II. Background

The low-order method developed for post-stall calculations by the NCSU Applied Aerodynamics Group uses the concept of viscous decambering to simulate the effects of a separated boundary layer. Decambering can be applied to an inviscid low-order method, such as lifting-line theory, Weissinger’s method, and two- and three-dimensional panel methods like the vortex lattice method (VLM), etc. to allow the inviscid theory to predict lift and moment in the post-stall regime.

II. A. Two-dimensional decambering method

At low angles of attack, the flow over the airfoil is fully attached, and the inviscid panel method accurately predicts the lift and moment on the airfoil. An increase in the angle of attack creates an adverse pressure gradient on the upper surface, causing flow separation and a drop in lift and an increase in nose-down pitching moment. This effect is modeled using a nonlinear decambering flap hinged at the separation point, having an angle δ_l at the hinge, and a height m at the trailing edge.

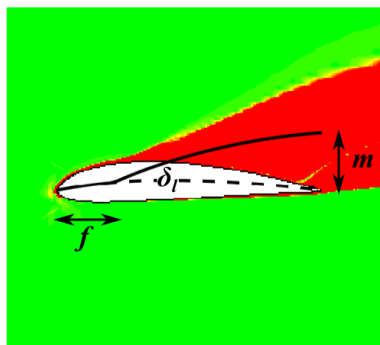


Figure 1: The nonlinear decambering flap and the decambering variables for the NACA 4415 airfoil at $\alpha = 18^\circ$

A viscous C_l vs α and C_m vs. α curve, obtained from CFD or experiment, is assigned to the airfoil. The separation location can be calculated using the Beddoes-Leishman equation for normal force on a thin airfoil experiencing separated flow. The separation curve for the NACA 4415 airfoil is shown in [Figure 2](#). The equations to calculate the decambering variables are quite sensitive to the location of the decambering flap hinge point, and as $f \rightarrow 1$, $\delta_l \rightarrow \pi/2$ and $m \rightarrow \infty$. To avoid this problem, the location of the hinge of the decambering flap is limited to 90% of chord.

$$C_n = 2\pi \sin(\alpha - \alpha_{0L}) \left(\frac{1 + \sqrt{f}}{2} \right)^2 \quad (1)$$

$$f = \left(\sqrt{\frac{2C_n}{\pi \sin(\alpha - \alpha_{0L})}} - 1 \right)^2 \quad (2)$$

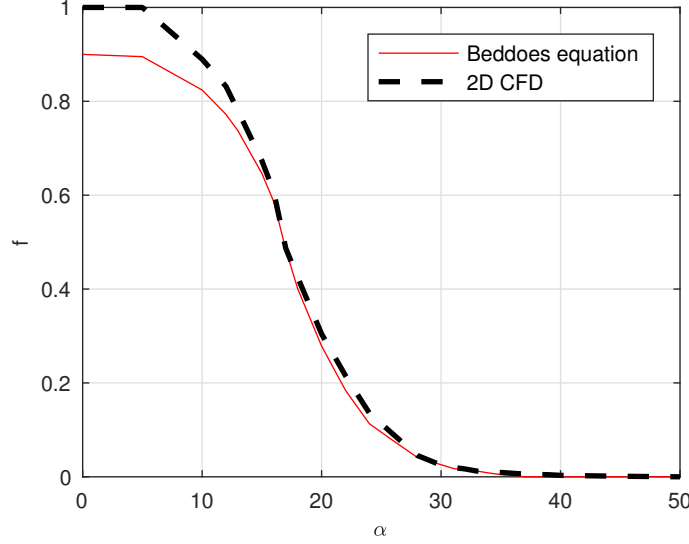


Figure 2: Separation point obtained from the Beddoes-Leishman equation and CFD

Next, a nonlinear flap hinged at f is applied to the geometry, such that the slope of the flap at the hinge is $\tan(\delta_l)$ and the height of the decambered camberline at the trailing edge is m . The following equations, obtained from thin-airfoil theory, relate the decambering variables (f, δ_l, m) to the desired drop in lift and moment coefficient.

$$\begin{bmatrix} m \\ \tan \delta_l \end{bmatrix} = \frac{1}{a_1 b_2 - a_2 b_1} \begin{bmatrix} p_1 & q_1 \\ p_2 & q_2 \end{bmatrix} \begin{bmatrix} b_2 & -b_1 \\ -a_2 & a_1 \end{bmatrix} \begin{bmatrix} \Delta C_l \\ \Delta C_m \end{bmatrix} \quad (3)$$

where,

$$p_1 = (1 - f)^2 + 2f(1 - f); \quad p_2 = f; \quad q_1 = 1 - f; \quad q_2 = 1$$

$$\begin{aligned} a_1 &= 3\theta_f - 3\pi - 4\sin\theta_f + \frac{\sin 2\theta_f}{2}; & a_2 &= \frac{3}{4}\sin\theta_f - \frac{3}{8}\sin 2\theta_f + \frac{\sin 3\theta_f}{12} - \frac{\theta_f}{4} + \frac{\pi}{4} \\ b_1 &= 2\theta_f - 2\pi - 2\sin\theta_f; & b_2 &= \frac{\sin\theta_f}{2} - \frac{\sin 2\theta_f}{4} \\ \theta_f &= \cos^{-1}(1 - 2f) \end{aligned}$$

Figure 3 shows the lift and moment obtained from CFD and the 2D panel method with nonlinear decambering. Figure 4 shows the variation of the flap angle and trailing-edge height needed to obtain the viscous curve from the inviscid curve. A detailed explanation of the nonlinear decambering method, and its application to 2D unsteady aerodynamics can be found in Ref. 19.

At low angles of attack, the flow is attached and the value of m is small. As the angle of attack increases, an upward flap deflection ($\delta_l < 0$) is required to simulate the drop in C_l . With a further increase in the angle of attack, the flap angle reaches close to 90° and the trailing-edge height increases exponentially.

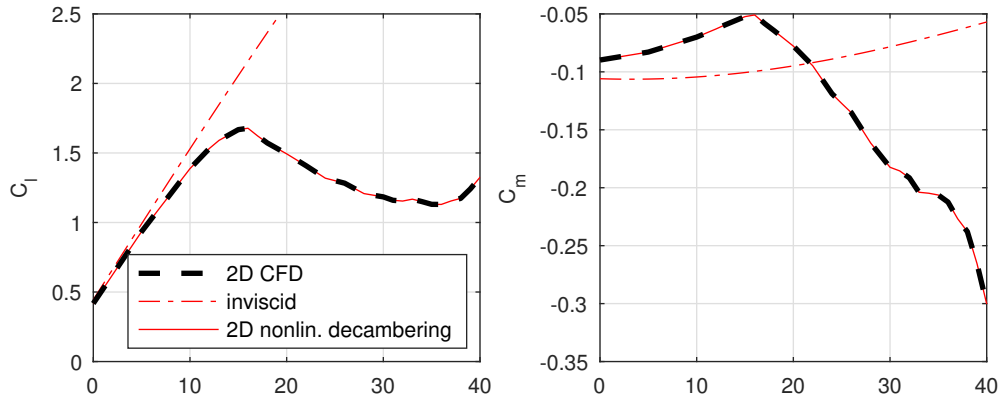


Figure 3: Lift and moment prediction by the 2D nonlinear decambering method compared to RANS CFD

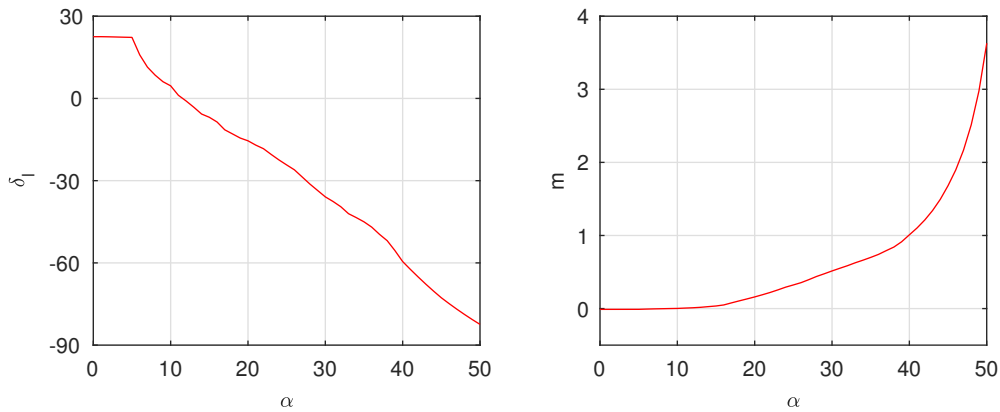


Figure 4: Variation of decambering flap angle δ_l and trailing-edge height m with angle of attack α

II. B. Three-dimensional nonlinear decambering

The nonlinear decambering method described above can be applied to a three-dimensional panel method such as the VLM to calculate pre- and post-stall loading on wings. The VLM implementation used in this work is described in detail by Katz and Plotkin.²⁰ The geometry is discretized into quadrilateral panels distributed over the camberline of each surface. Vortex rings are then assigned to each panel, such that the leading segment of each ring lies on the quarter-chord line of the panel. A collocation point, where the zero-normal-flow boundary condition is enforced, is placed at the three-quarter-chord and semi-span point of each panel. The current implementation assumes a flat, steady wake extending downstream to infinity.

In addition to the geometry discretization, each section is assigned a f vs. α_{eff} , δ_l vs. α_{eff} , and m vs. α_{eff} curve obtained from the 2D decambering method. Starting with no decambering at any section ($\delta_l = 0, m = 0$), the VLM is solved to obtain the spanwise lift distribution, and hence the local effective angle of attack (α_{eff}) at each section. Since each section must behave like the airfoil, target C_l and C_m distributions are obtained from the viscous curves of the airfoil. A set of decambering variables is obtained for each section from the assigned f , δ_l , and m vs. α_{eff} curves. The geometry is modified by applying this decambering flap, and the VLM is executed to obtain the next iteration of the solution. Due to 3D effects, applying a decambering flap affects the α_{eff} of every section. A new set of decambering variables can be obtained from this new α_{eff} distribution. This process is repeated until the difference between the target solution and the actual solution is within a specified tolerance. A tolerance of 0.05 was used for the maximum error in C_l . **Figure 5** compares the predictions from the low-order method and CFD for CL and CM about quarter chord for an unswept wing of $\mathcal{R} = 12$ at $0^\circ \leq \alpha \leq 30^\circ$. **Figure 6** shows a comparison of the spanwise distributions of lift and moment at a post-stall angle of attack ($\alpha = 18^\circ$).

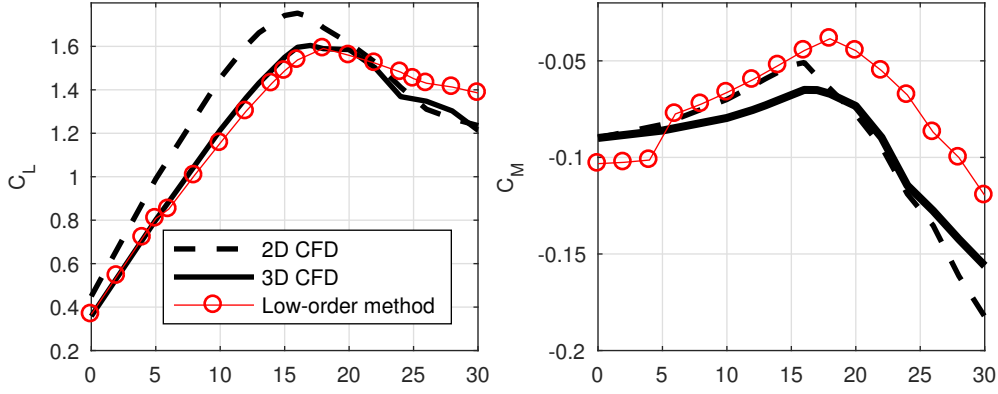


Figure 5: Lift and moment prediction by the 3D nonlinear decambering method compared to RANS CFD for an unswept $\mathcal{R} = 12$ wing

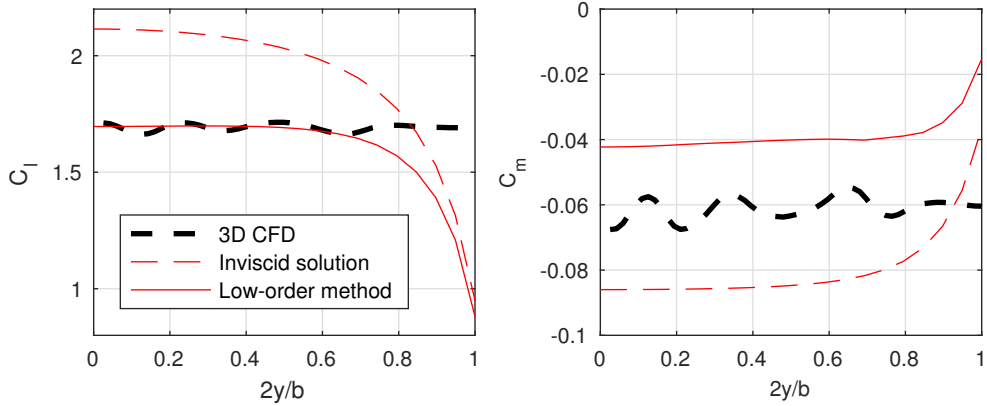


Figure 6: Spanwise variations of lift and moment predicted by the 3D nonlinear decambering method compared to RANS CFD for an unswept $\mathcal{R} = 12$ wing at $\alpha = 18^\circ$

II. C. Nonlinear decambering for swept wings

The flow over a section of a rectangular wing is largely two-dimensional. However, in the case of swept wings, a transverse pressure gradient exists that induces a spanwise component in the flow. Since the flow is no longer locally two-dimensional, the sections of a swept wing behave differently from the airfoil. Compared to the airfoil, sections near the root experience attached flow upto higher α , and stall is delayed, whereas outboard sections experience advanced flow separation and stall at lower α .²¹ This behavior was characterized for NACA 4415 wings with $\mathcal{R} = 12$ by Hosangadi et al.¹⁷

The nonlinear decambering input (f, δ_l, m vs. α_{eff}) must be modified to account for this behavior for accurate prediction of the loads on swept wings. The decambering input curves for each section of a swept wing are generated by using the method described in Ref. 17 to obtain modified C_l curves to use as viscous input curves in the 2D decambering method. The spanwise variation in C_m behavior due to the effects of sweep is calculated using the modified lift curve of the section and the C_m/C_l curve of the airfoil. Figure 7 compares the lift and moment predictions from the decambering method for a 20° swept wing of $\mathcal{R} = 16$ with CFD solutions. The spanwise loading at a post-stall $\alpha = 18^\circ$ is shown in Figure 8

II. D. Wake prediction

Although the decambering method predicts the post-stall wing loading fairly well, it does not include any boundary-layer calculations. A velocity field calculated by adding the velocities induced by every bound

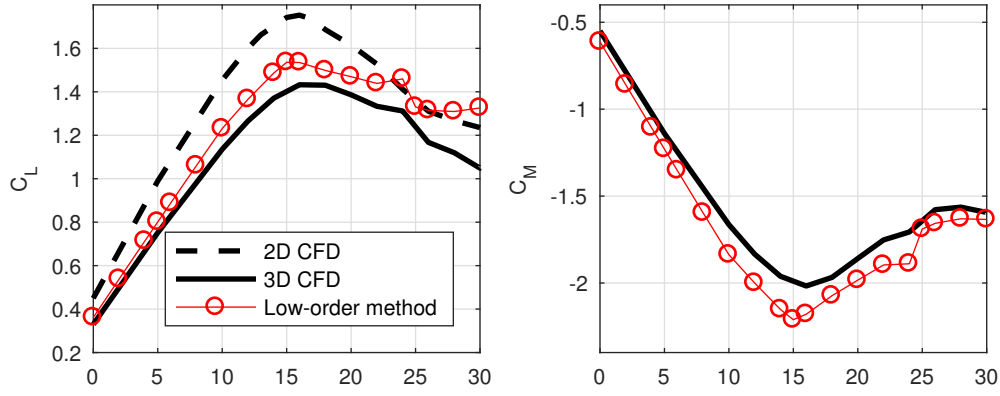


Figure 7: Lift and moment about root-quarter-chord predicted by the 3D nonlinear decambering method compared to RANS CFD for a 20° swept $\mathcal{R}16$ wing

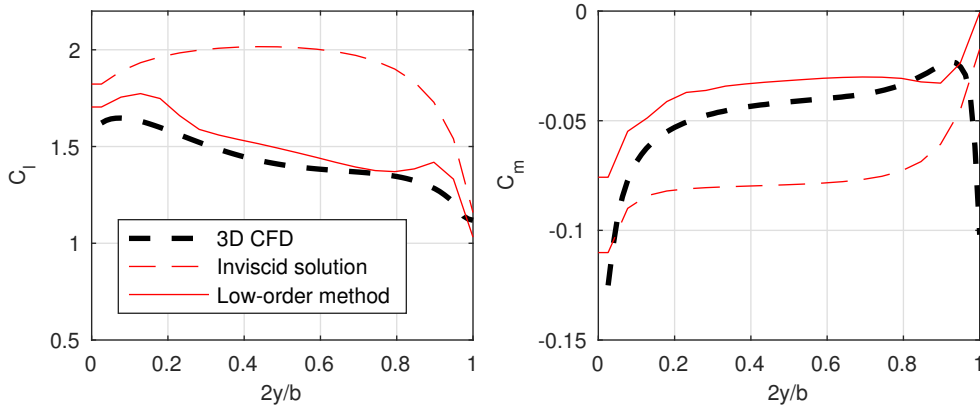


Figure 8: Spanwise variation of lift and quarter-chord-moment coefficients predicted by the 3D nonlinear decambering method compared to RANS CFD for a 20° swept $\mathcal{R} = 16$ wing at $\alpha = 18^\circ$

and wake vortex shows no velocity deficit behind the wing. Without a viscous boundary layer, the effects of wake impingement on downstream surfaces is not correctly modeled. This makes the decambering method, in its current form, unsuitable for use in applications where wake impingement is important, such as in a post-stall flight simulator. The following section describes a methodology to address this shortcoming of the decambering method

III. Methodology

The VLM, augmented with the decambering method, has been shown to calculate the loads on the wing reasonably well. In doing so, the circulation distribution over the wing is calculated, and the total velocity at any point in the flow field can be calculated as the sum of the velocity induced by every vortex structure and V_∞ . The velocity field thus obtained is used to estimate the location of the centerline of the wake using a streamline that originates at the center of the wake at the trailing edge. The variation of the velocity in the wake is obtained from the empirical relations given by Silverstein et al.²²

III. A. Wake width and velocity deficit

The velocity deficit in the wake can be calculated from the profile drag of the wing section.²³

$$F_d = \rho \int_{-\infty}^{\infty} v(V_{\infty} - v)dz \quad (4)$$

From Equation (4) and experimental data, Silverstein et al. derived an empirical relation for the velocity profile in the wake:²²

$$\eta = \frac{2.42 C_{d_0}^{1/2}}{\xi + 0.3} \quad (5)$$

$$\frac{\eta'}{\eta} = \cos^2 \frac{\pi \zeta'}{2\zeta} \quad (6)$$

$$\zeta = 0.68 C_{d_0}^{1/2} (\xi + 0.15)^{1/2} \quad (7)$$

where

$$\begin{aligned} \eta &= \frac{\text{dynamic pressure loss at centerline of wake}}{\text{dynamic pressure in free stream}} = \frac{\Delta q}{q_{\infty}} = 1 - \frac{q}{q_{\infty}} \\ \frac{\eta'}{\eta} &= \frac{\text{dynamic pressure loss at any point in the wake}}{\text{dynamic pressure loss at wake centerline}} \\ \zeta &= \frac{1}{2} \frac{\text{wake width}}{\text{wing chord}} = \frac{B}{2c}; -1 \leq \frac{\zeta'}{\zeta} \leq 1 \\ \xi &= \frac{\text{distance behind trailing edge}}{\text{wing chord}} = \frac{x - x_{TE}}{c} \end{aligned}$$

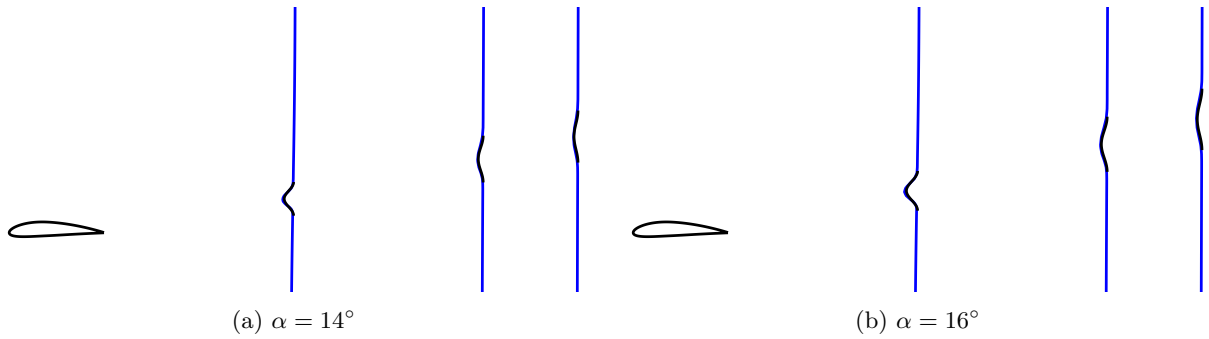
These equations can be rewritten to get the velocity at any point in the wake:

$$\frac{V}{V_{\infty}}(\xi, \zeta'/\zeta, C_d) = \sqrt{1 - \frac{2.42 C_d^{0.5}}{\xi + 0.3} \cos^2 \left(\frac{\pi}{2} \frac{\zeta'}{\zeta} \right)} \quad (8)$$

The local C_d of the section is obtained by multiplying its local C_l with the C_d/C_l of the airfoil. This accounts for the change in local section behavior due to wing sweep. Equation (8) applies at pre- and post-stall conditions, since the increase in C_d accounts for the increase in wake width and velocity deficit.

III. B. Validation with airfoil CFD results

To verify that the empirical relations given by Silverstein et al. hold for the NACA 4415 airfoil, the velocity deficit in the wake was calculated and compared with 2D CFD solutions. Figure 9 shows the predicted velocity profile in the wake, overlaid on the velocity profile obtained from the CFD solution at three chordwise stations 2, 4, and 5 chord-lengths aft of the trailing edge. Wake deficit predictions agree well with CFD results.



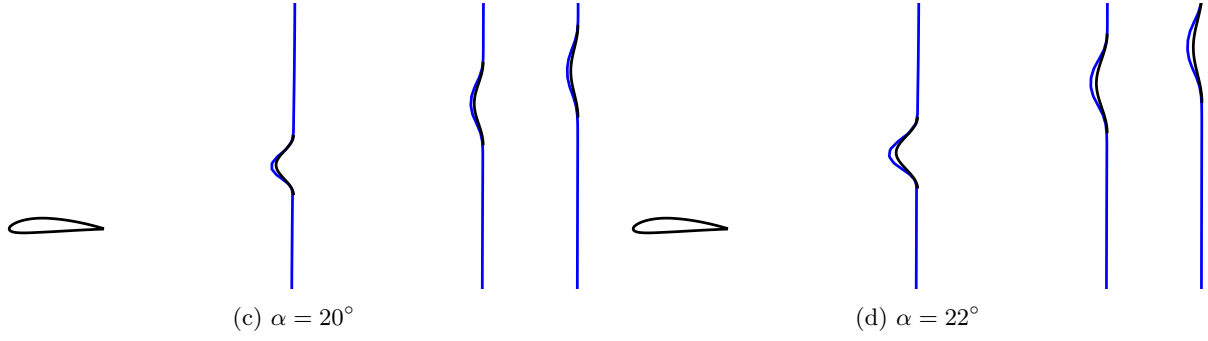


Figure 9: Velocity deficit in the wake of the NACA 4415 airfoil from CFD (blue) and semi-empirical equations (black)

III. C. Prediction of wake centerline

The total velocity at any point in the flow field is the sum of the velocities induced by every bound vortex ring in the geometry, every horseshoe vortex in the wake, and V_∞ .

$$\vec{V}_p = \vec{V}_\infty + \sum_{i=1}^{N_{bound}} \vec{v}_i \Gamma_i + \sum_{j=1}^{N_{wake}} \vec{v}_j \Gamma_j \quad (9)$$

where \vec{v}_i denotes the velocity induced by a bound vortex ring of unit strength, and \vec{v}_j denotes the velocity induced by a wake vortex of unit strength. This can be represented by an influence coefficient matrix:

$$\mathbf{V}_x = [VIC_x] \mathbf{\Gamma}_{bound} + [VIC_x] \mathbf{\Gamma}_{wake} \quad (10)$$

$$\mathbf{V}_y = [VIC_y] \mathbf{\Gamma}_{bound} + [VIC_y] \mathbf{\Gamma}_{wake} \quad (11)$$

$$\mathbf{V}_z = [VIC_z] \mathbf{\Gamma}_{bound} + [VIC_z] \mathbf{\Gamma}_{wake} \quad (12)$$

$$\mathbf{V} = \mathbf{V}_x \hat{i} + \mathbf{V}_y \hat{j} + \mathbf{V}_z \hat{k} + \vec{V}_\infty \quad (13)$$

Since these influence coefficient matrices depend solely on the geometry, they are calculated once per geometry and reused.

The nonlinear decambering approach applies a quadratic trailing-edge flap hinged at the location of the separation point f , and which has an angle δ_l at the separation location, and a height m above the trailing edge. Since the flap models trailing-edge separation, its height above the trailing edge is used as a substitute for the mid-point of the wake. A streamline is calculated starting at this point $(x_{TE}, y_{TE}, m \cdot c + z_{TE})$, using the velocity field calculated in the previous step. This streamline is used as a low-order estimate of the location of the wake centerline.

III. D. Geometries studied

The current work focuses on the wake behind an unswept NACA 4415 wing with $\mathcal{R} = 12$ and a 20° swept NACA 4415 wing of $\mathcal{R} = 16$. The tail is not included in the calculations, but one is shown 5.5 chord lengths behind the trailing edge of the wing and 1.2 chord lengths above the z plane to illustrate the approximate location of the tail in a generic T-tail commuter-aircraft configuration. Velocities induced by the vortex lattice are calculated at a grid of points between the wing and tail. [Section IV](#) presents the results obtained using a 10×10 grid behind the wing.

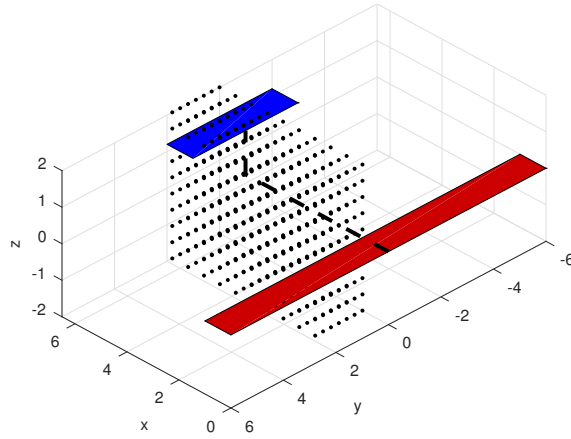


Figure 10: Locations at which velocities are calculated for the unswept wing

IV. Results

The results obtained from the method described above are presented in the following sections. First, we compare the centerline and width of the wake predicted by the low-order method with CFD solutions. The plots in this section are formatted as follows: The centerline of the wake, as predicted by the low-order method, is denoted by a dashed blue line. The translucent white patch denotes the extent of the wake. This is overlaid on a vorticity contour plot from CFD solutions. The region of high vorticity, shown here in red, denotes the wake extent as calculated by CFD. The decambered camberline of the section is plotted over the airfoil

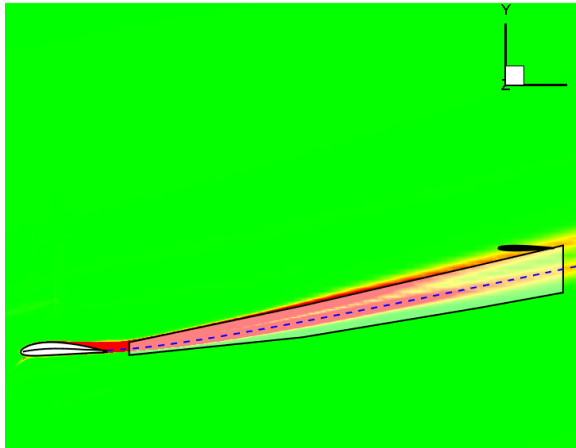
Next, the predicted velocity deficit in the wake is compared to CFD solutions. In these plots, the velocity profile obtained from CFD at multiple chordwise stations 2, 4, and 5 chords behind the trailing edge is shown using a blue line. The black line denotes the velocity profile predicted using the method described above at the same chordwise stations. Results are presented for the $\mathcal{R}12$ unswept wing and $\mathcal{R}16, 20^\circ$ swept wing at angles of attack before and after stall, and at inboard spanwise locations such that $y < b_{\text{tail}}/2$.

At most sections, the low-order predictions agree satisfactorily with CFD solutions. Some predictions of the wake centerline differ significantly from the CFD solution, e.g. $y = 1.5, \alpha = 20^\circ$. In this case, the decambered trailing edge is not close to the midpoint of the wake. Additional research is required to improve the 3D decambering method and correct these discrepancies.

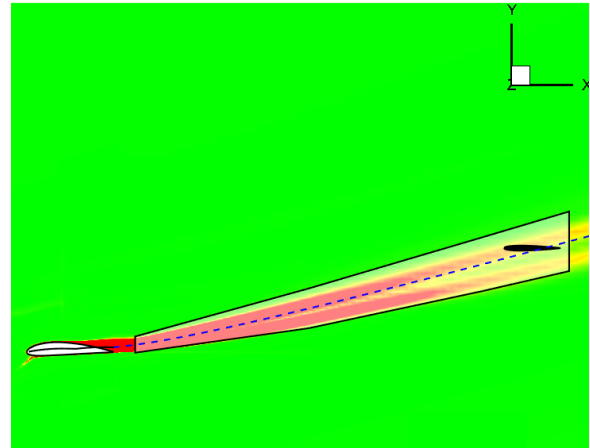
IV. A. Rectangular wing

This section contains selected images comparing the wake centerline, width, and velocity deficit predictions from the low order method with CFD solutions for the $\mathcal{R}12$ rectangular wing.

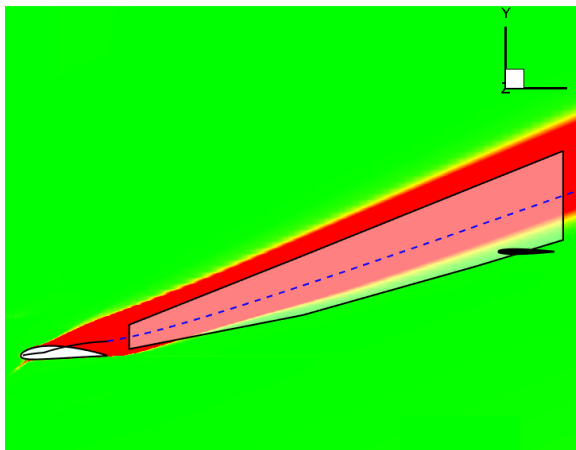
1. *Wake centerline and width*



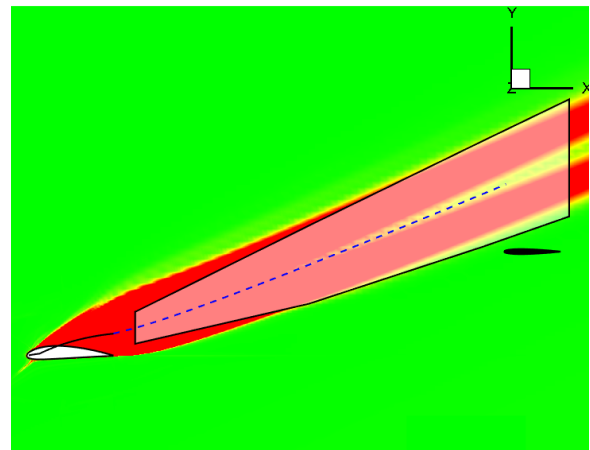
(a) $\alpha = 15^\circ$



(b) $\alpha = 18^\circ$

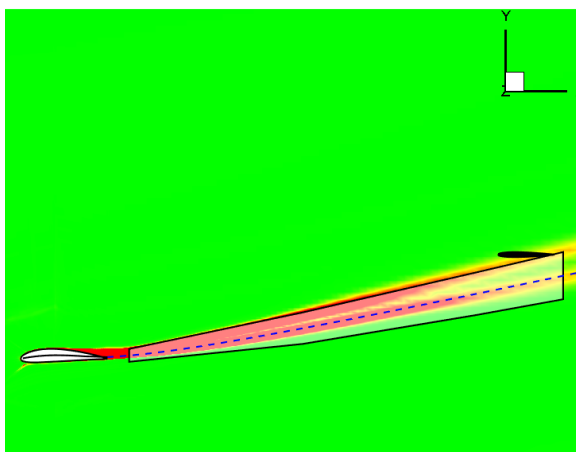


(c) $\alpha = 22^\circ$

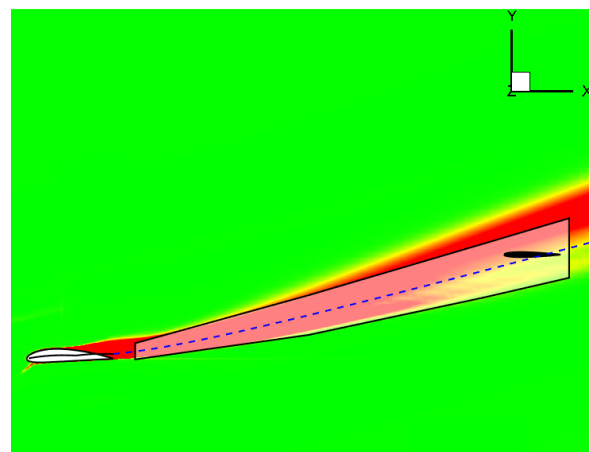


(d) $\alpha = 25^\circ$

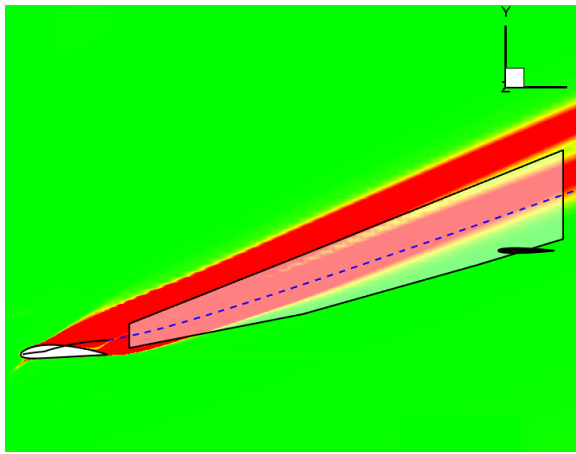
Figure 11: Wake prediction at $y = 0.3$



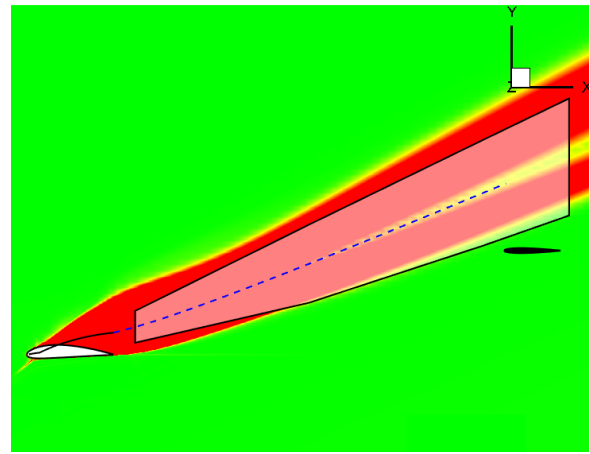
(a) $\alpha = 15^\circ$



(b) $\alpha = 18^\circ$

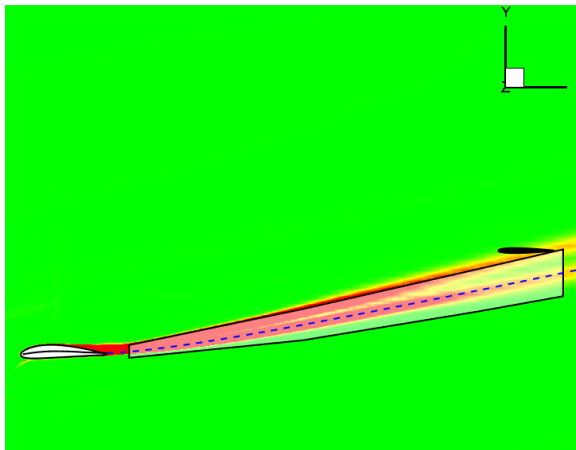


(c) $\alpha = 22^\circ$

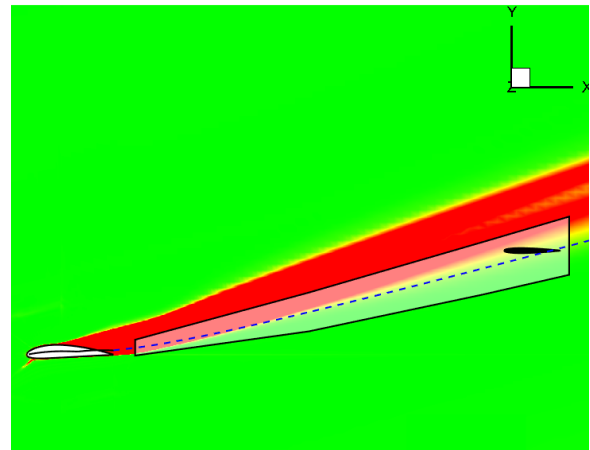


(d) $\alpha = 25^\circ$

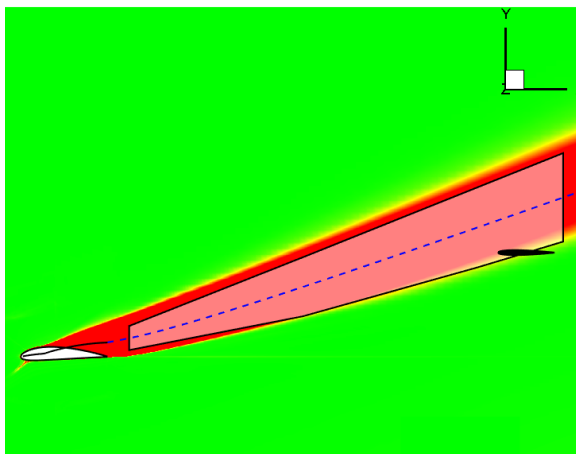
Figure 12: Wake prediction at $y = 0.6$



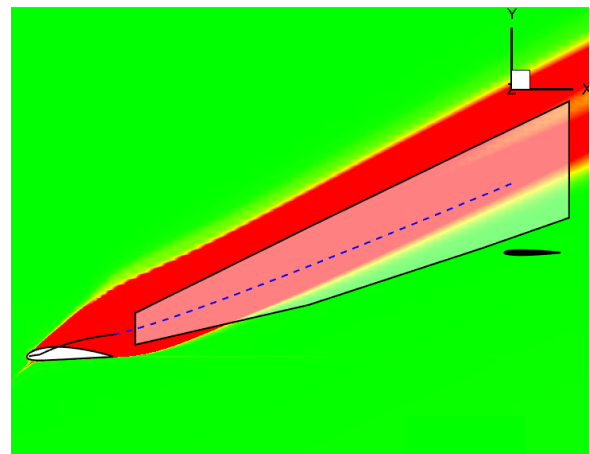
(a) $\alpha = 15^\circ$



(b) $\alpha = 18^\circ$

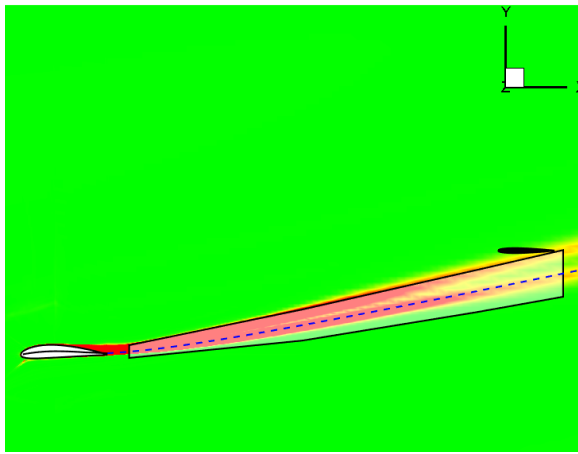


(c) $\alpha = 22^\circ$

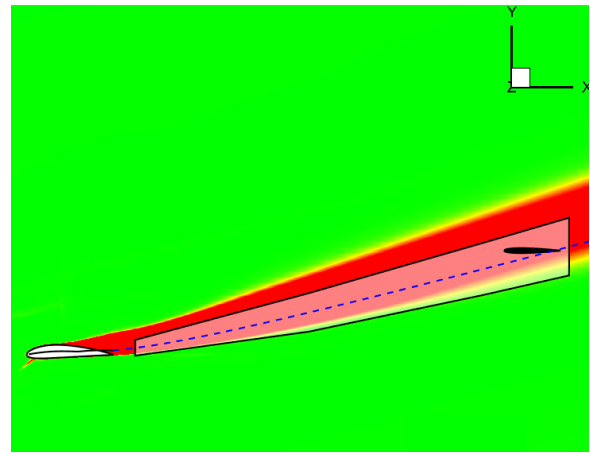


(d) $\alpha = 25^\circ$

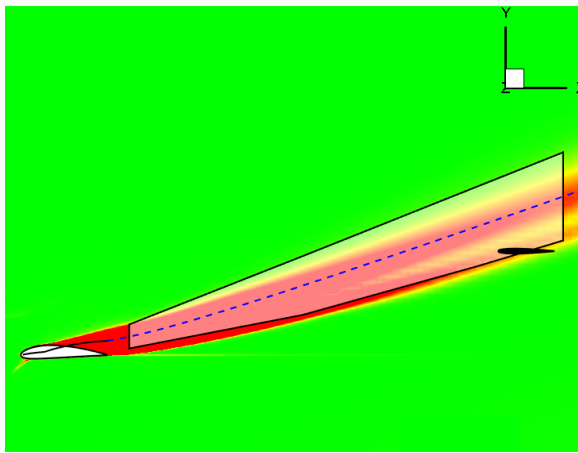
Figure 13: Wake prediction at $y = 1.5$



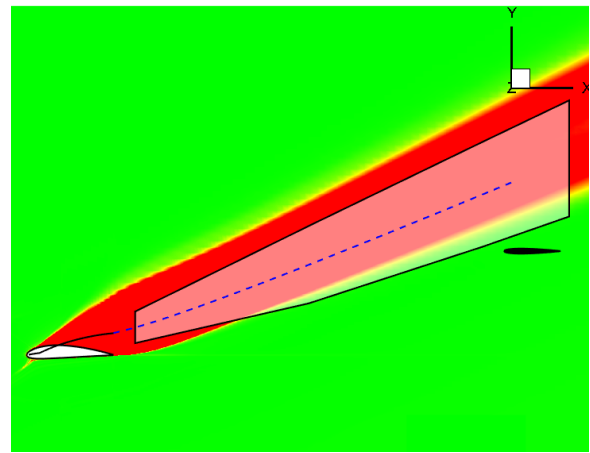
(a) $\alpha = 15^\circ$



(b) $\alpha = 18^\circ$



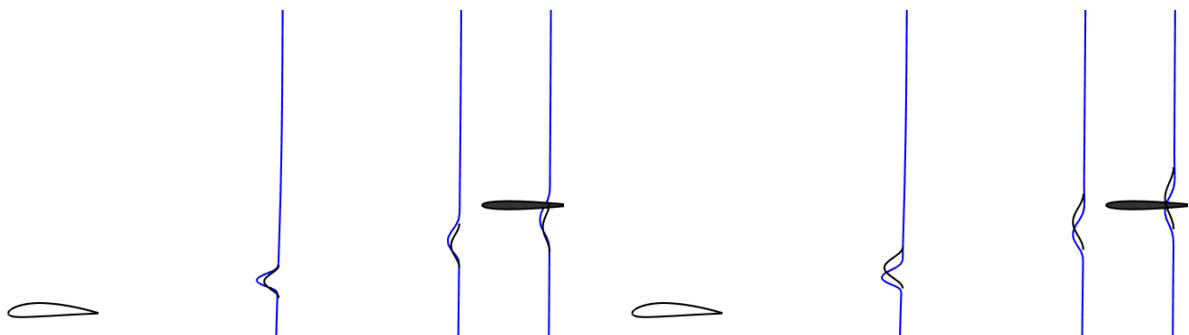
(c) $\alpha = 22^\circ$



(d) $\alpha = 25^\circ$

Figure 14: Wake prediction at $y = 1.8$

2. Wake velocity deficit



(a) $\alpha = 15^\circ$

(b) $\alpha = 18^\circ$

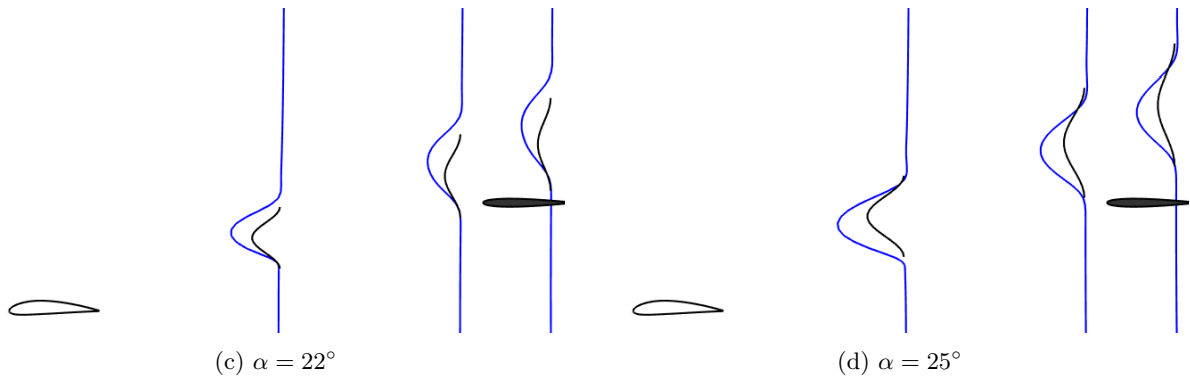


Figure 15: Velocity deficit in the wake at $y = 0.3$

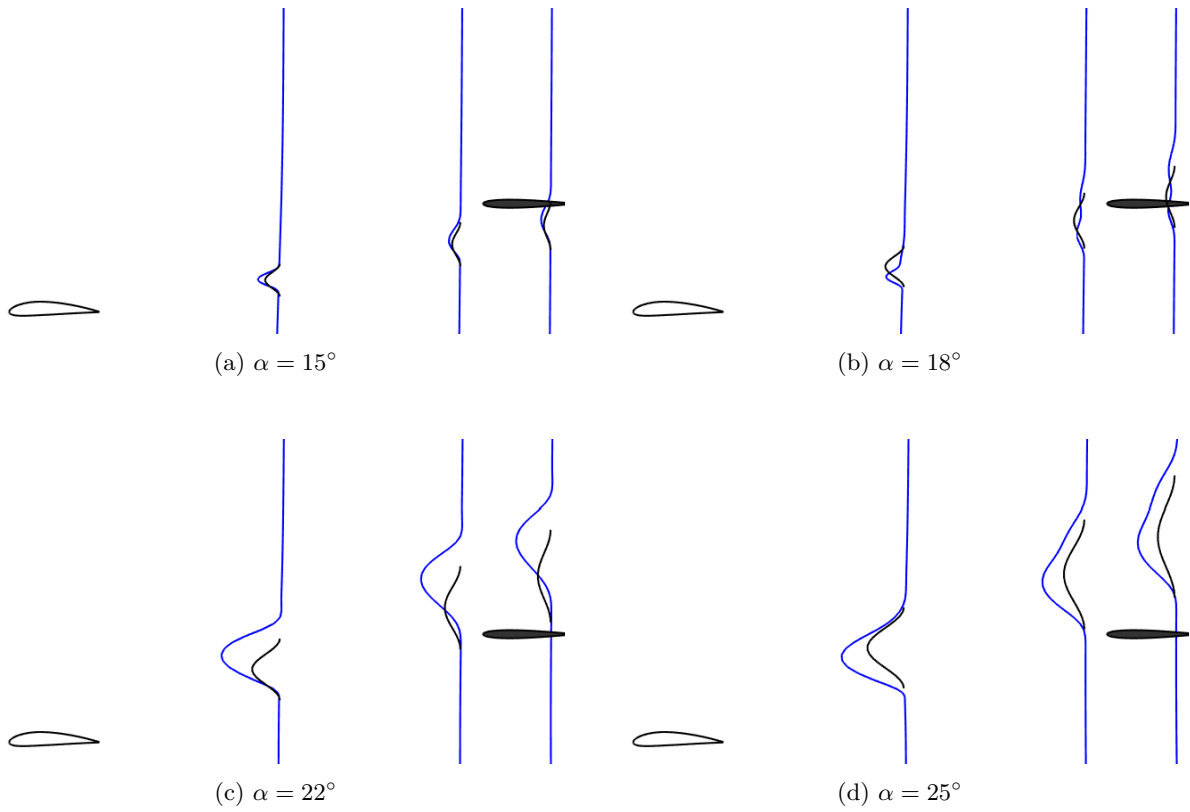


Figure 16: Velocity deficit in the wake at $y = 0.6$

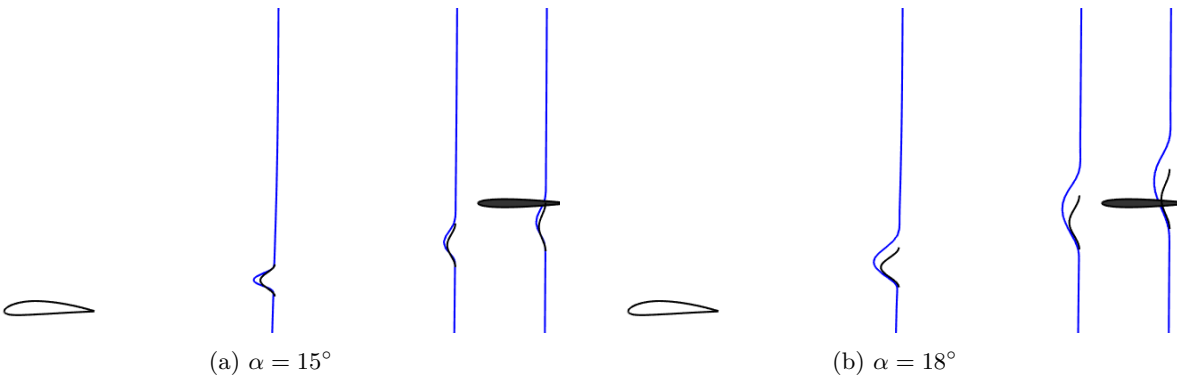


Figure 17: Velocity deficit in the wake at $y = 1.5$

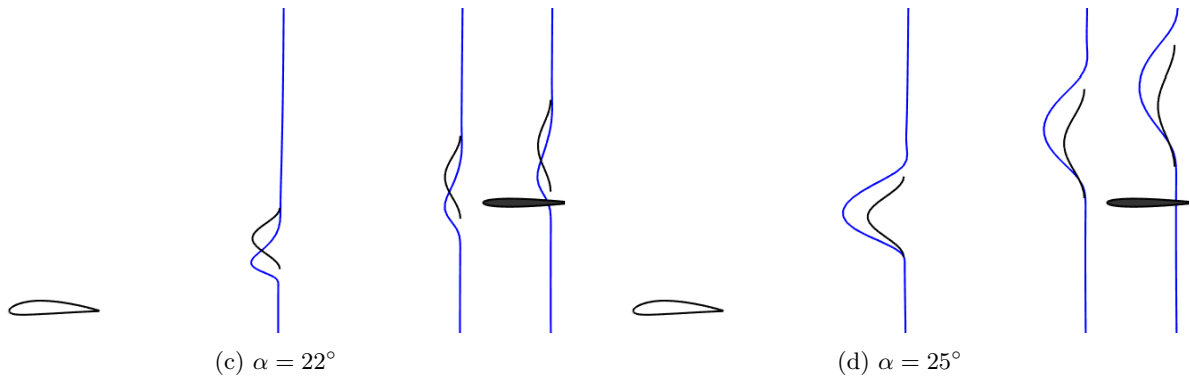
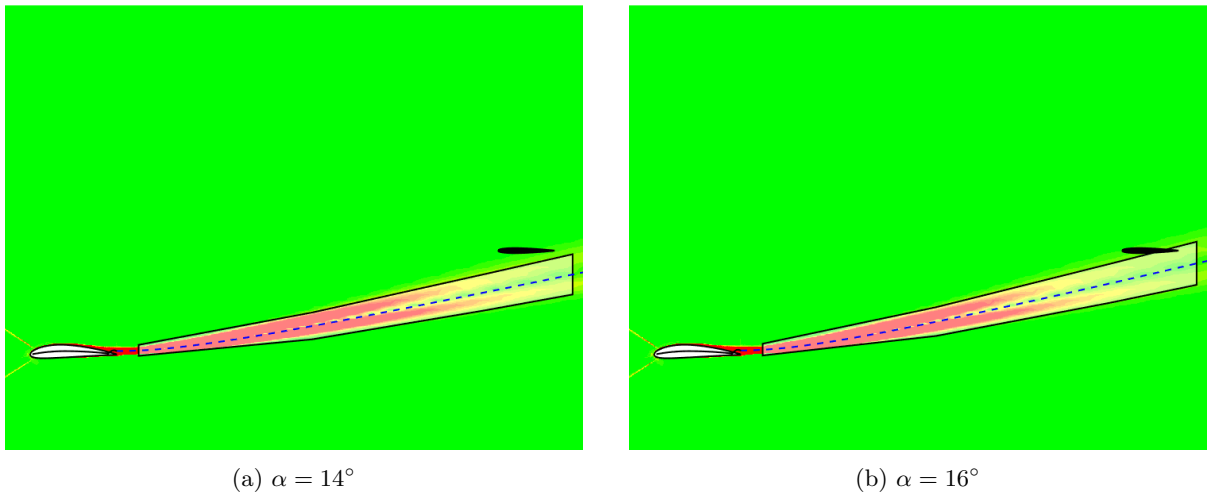


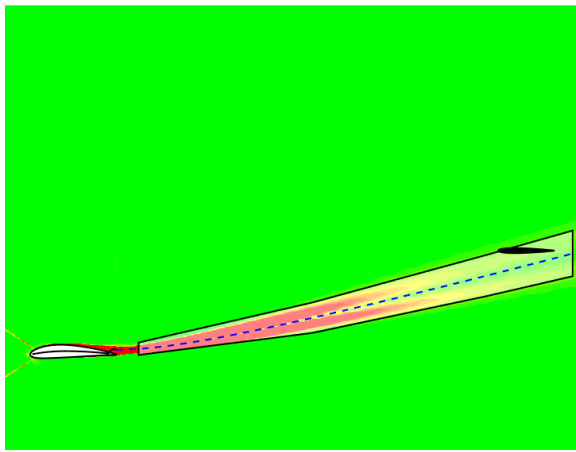
Figure 18: Velocity deficit in the wake at $y = 1.8$

IV. B. 20° swept wing

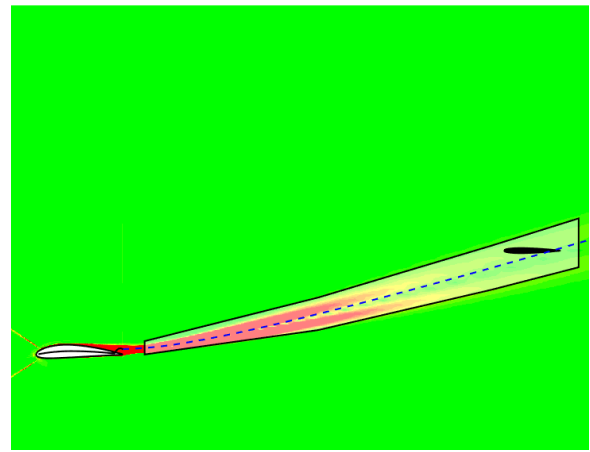
This section contains selected images comparing the wake centerline, width, and velocity deficit predictions from the low order method with CFD solutions for the $\mathcal{R}16$, 20° swept wing.

1. Wake centerline and width



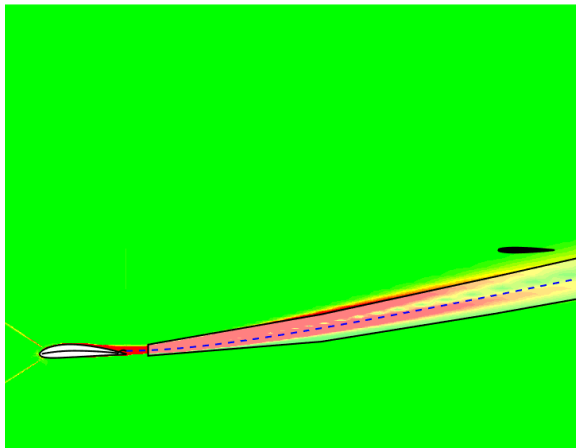


(c) $\alpha = 18^\circ$

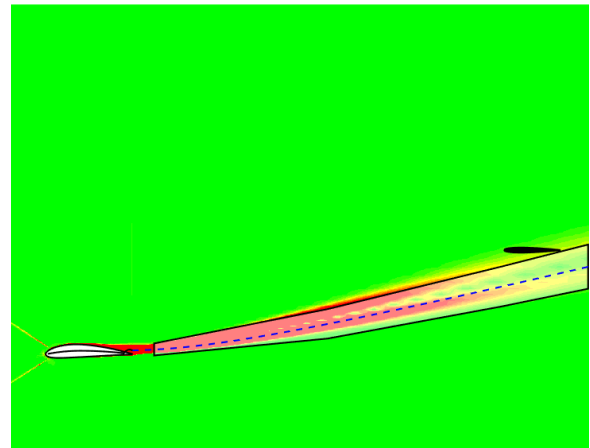


(d) $\alpha = 20^\circ$

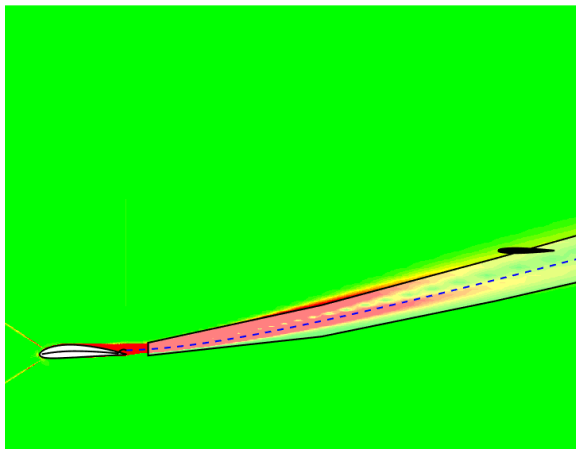
Figure 19: Wake prediction at $y = 0.3$



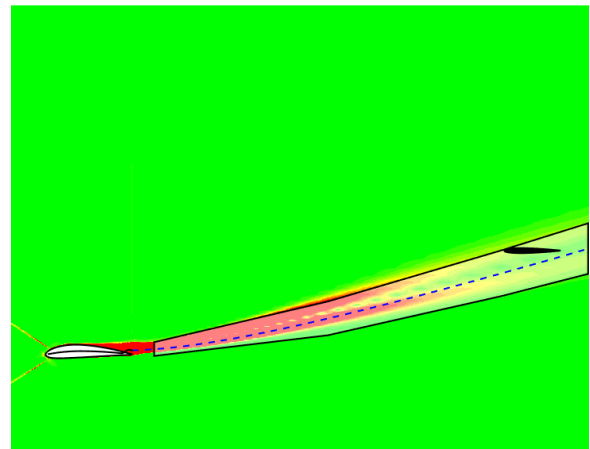
(a) $\alpha = 14^\circ$



(b) $\alpha = 16^\circ$

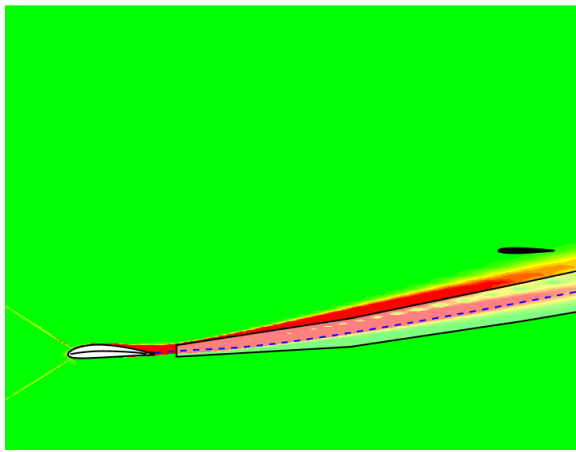


(c) $\alpha = 18^\circ$

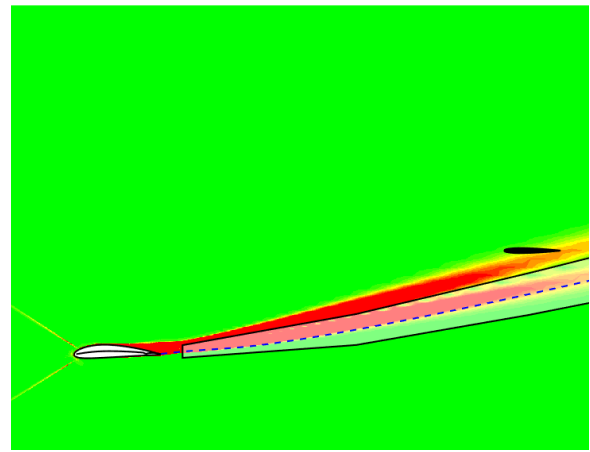


(d) $\alpha = 20^\circ$

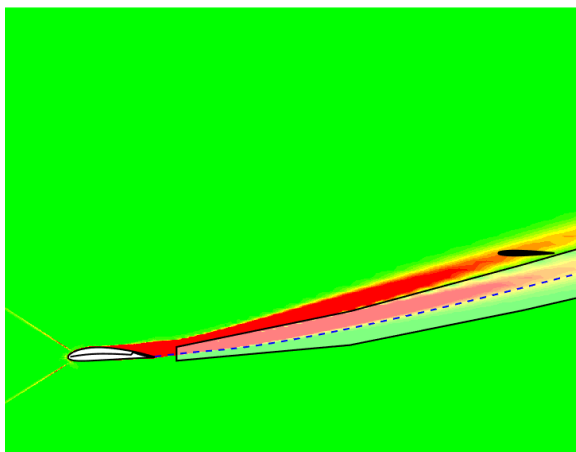
Figure 20: Wake prediction at $y = 0.6$



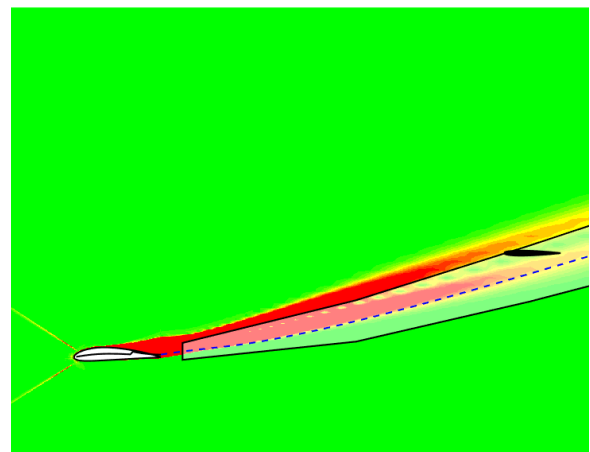
(a) $\alpha = 14^\circ$



(b) $\alpha = 16^\circ$

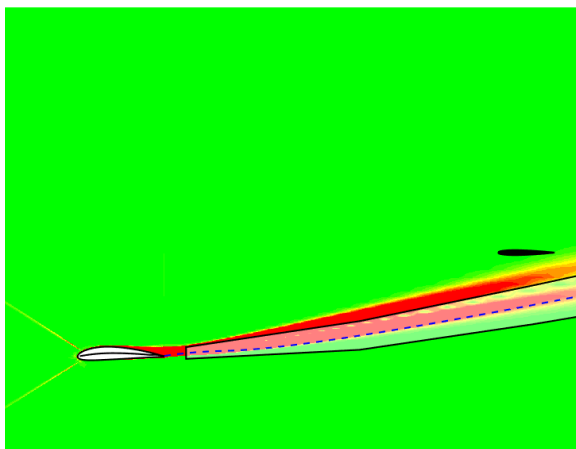


(c) $\alpha = 18^\circ$



(d) $\alpha = 20^\circ$

Figure 21: Wake prediction at $y = 1.5$



(a) $\alpha = 14^\circ$



(b) $\alpha = 16^\circ$

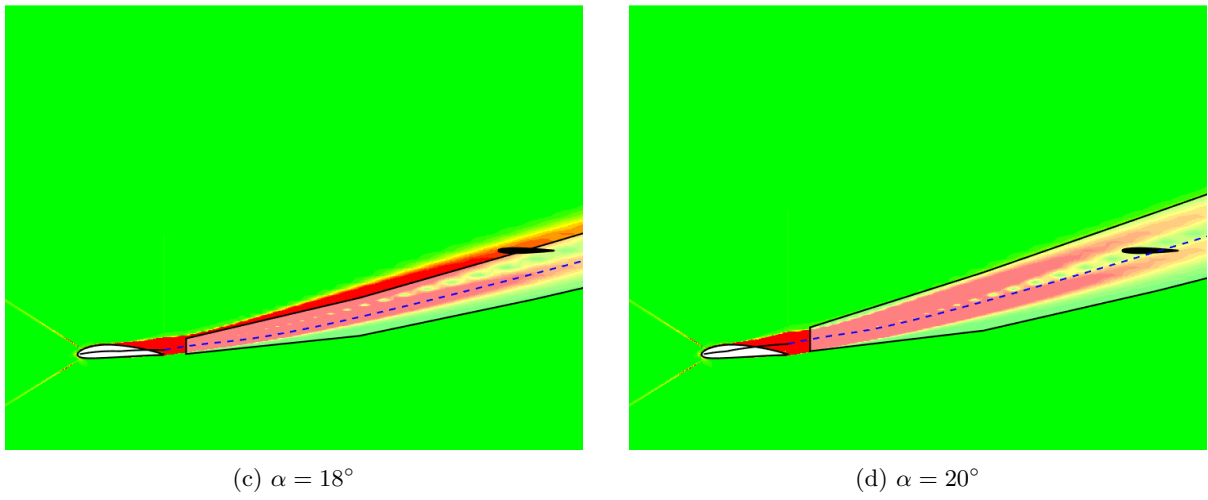


Figure 22: Wake prediction at $y = 1.8$

2. Wake velocity deficit

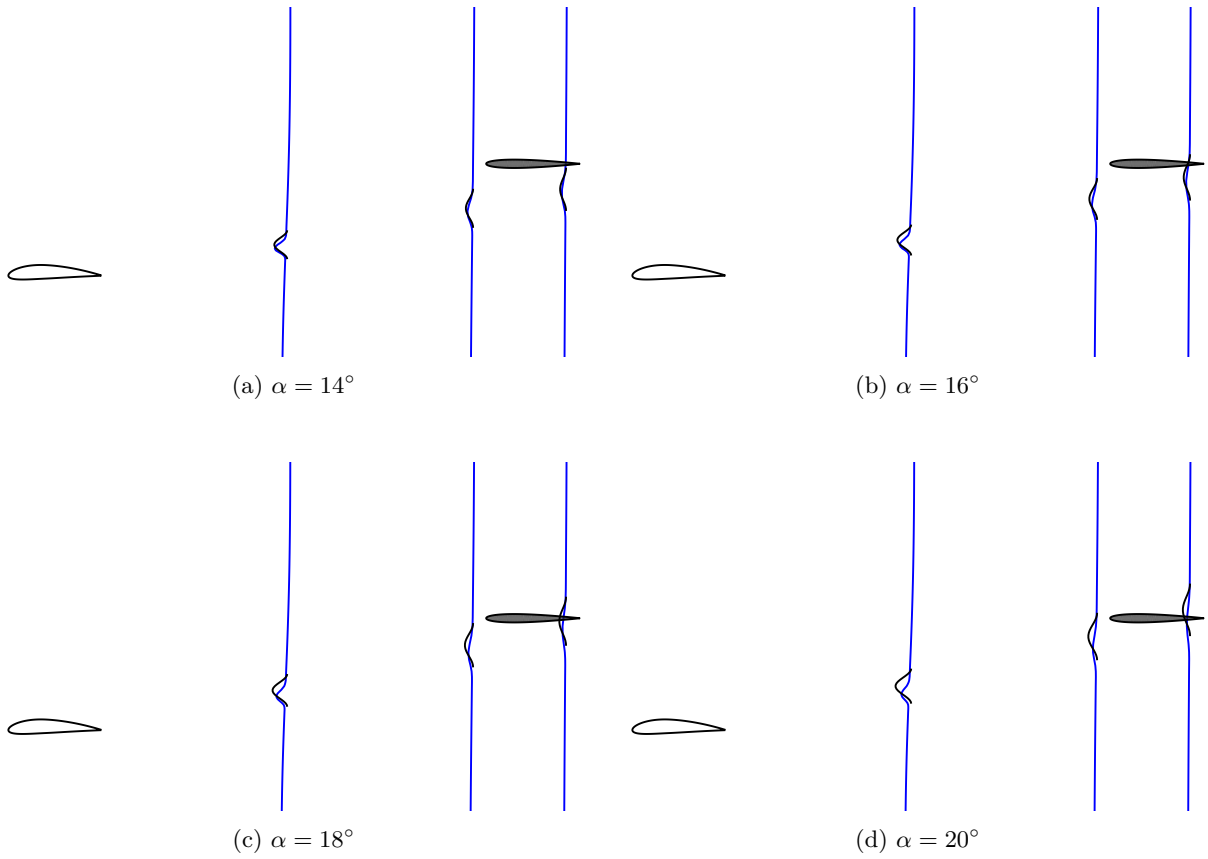


Figure 23: Velocity deficit in the wake at $y = 0.3$

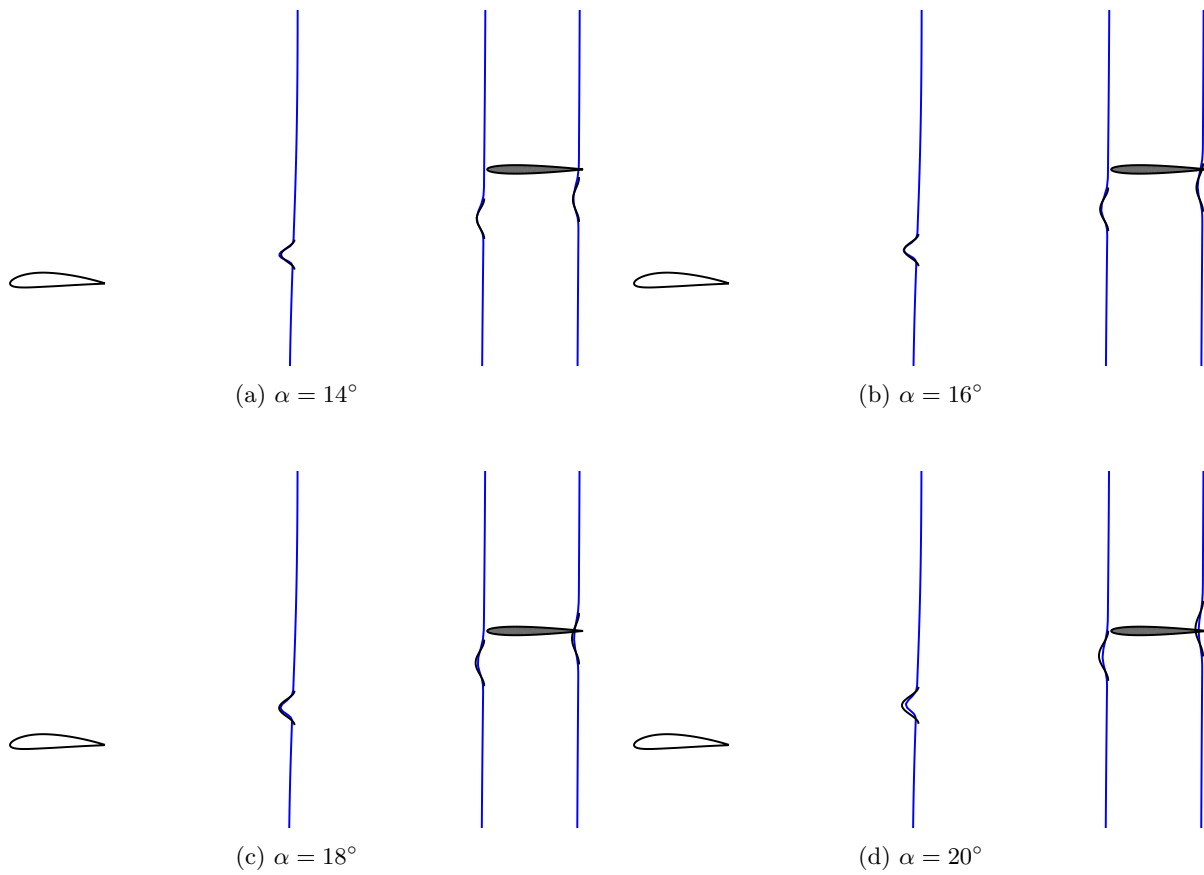
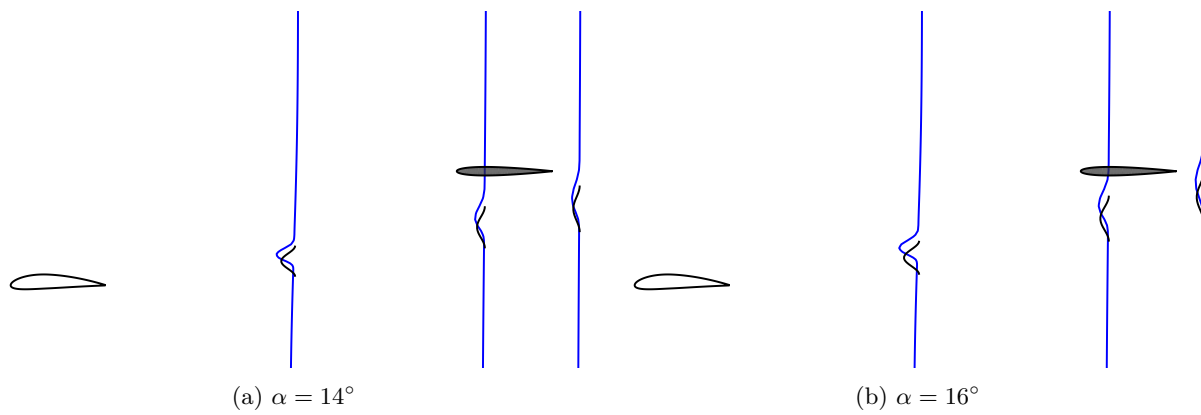


Figure 24: Velocity deficit in the wake at $y = 0.6$



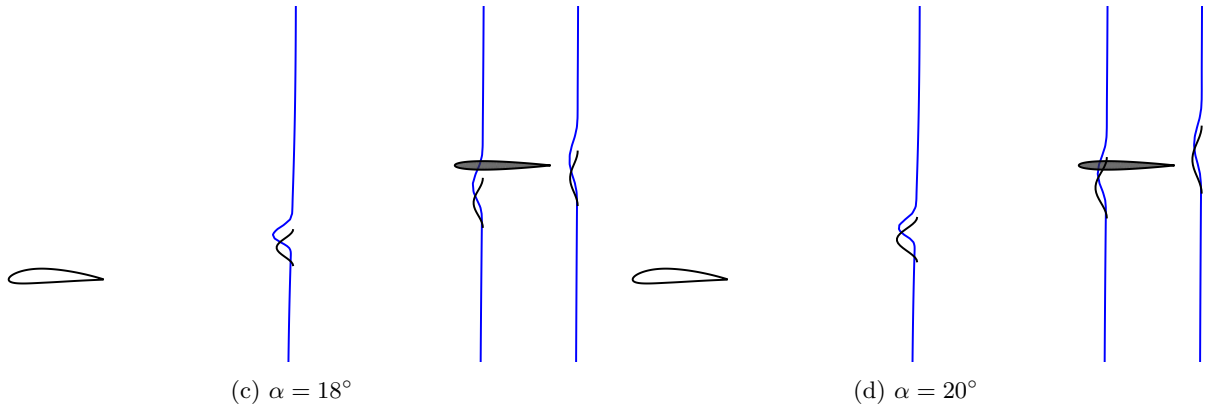


Figure 25: Velocity deficit in the wake at $y = 1.5$

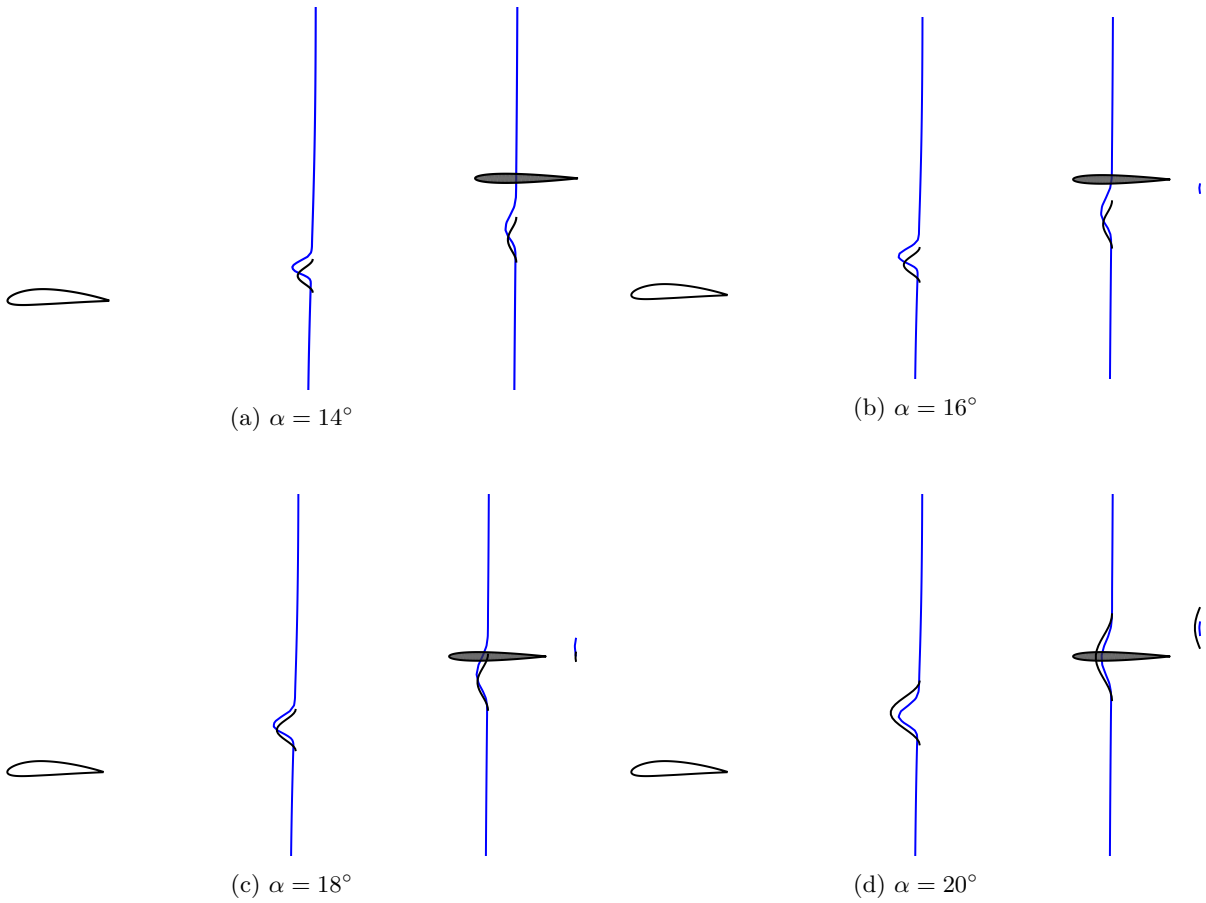


Figure 26: Velocity deficit in the wake at $y = 1.8$

V. Conclusions

This paper presents a methodology to augment a low-order decambering method to predict the location and width of the viscous wake behind a lifting surface, and the velocity deficit in the wake. It is shown that centerline of the wake can be predicted using a streamline derived from the inviscid vortex-induced velocity field behind the wing, and starting at the midpoint of the wake at the trailing edge of the section. Wake width and velocity deficit predictions are made using the section C_d , which is the local C_l of the section

multiplied by the C_d/C_l of the airfoil at the local section angle of attack. A new method of decambering, called “nonlinear decambering” is introduced. This method applies a nonlinear trailing-edge flap hinged at the separation point f , at an angle δ_l and having a height m above the trailing edge. The midpoint of the wake at the trailing edge is estimated using the trailing-edge height (m) from the nonlinear decambering method. Low-order predictions for the wake centerline, width and velocity deficit for an unswept and a swept wing were compared with corresponding CFD results. The comparisons are very good for most cases. The accuracy of the wake centerline prediction relies on a good estimate for m , and the quality of the prediction suffers at sections where m is not close to the midpoint of the wake. While more work is required to improve the prediction of m , the results presented in this work provide an excellent starting point to model the effects of the wake on downstream surfaces in the low-order method.

Acknowledgments

This research effort was supported by a grant from the NASA Langley Research Center under the Vehicle Systems Safety Technologies project. We thank technical monitors Gautam Shah and Neal Frink of NASA Langley, for their support and collaboration. We also thank Abhimanyu Jamwal of the NCSU Applied Aerodynamics Group for the CFD results used in this work.

References

- ¹Purser, P. E. and Spearman, M. L., “Wind-tunnel Tests at Low Speed of Swept and Yawed Wings Having Various Planforms,” NACA Technical Note 2445, National Advisory Committee for Aeronautics, 1951.
- ²Tseng, J. B. and Lan, C. E., “Calculation of Aerodynamic Characteristics of Airplane Configurations at High Angles of Attack,” NASA CR 4182, 1988.
- ³van Dam, C. P., Kam, J. C. V., and Paris, J. K., “Design-Oriented High-Lift Methodology for General Aviation and Civil Transport Aircraft,” *Journal of Aircraft*, Vol. 38, No. 6, November–December 2001, pp. 1076–1084.
- ⁴Anderson, J. D., Corda, S., and VanWie, D. M., “Numerical Lifting Line Theory Applied to Drooped Leading-Edge Wings Below and Above Stall,” *Journal of Aircraft*, Vol. 17, No. 12, 1980, pp. 898–904.
- ⁵Owens, B., “Weissinger’s Model of the Nonlinear Lifting Line Method for Aircraft Design,” AIAA Paper 98-0597, January 1998.
- ⁶Levinsky, E. S., “Theory of Wing Span Loading Instabilities Near Stall,” AGARD Conference Proceedings No. 204, September 1976.
- ⁷McCormick, B. W., “An Iterative Non-Linear Lifting Line Model for Wings with Unsymmetrical Stall,” *SAE Transactions Paper No. 891020*, 1989, pp. 91–98.
- ⁸Piszkin, S. T. and Levinsky, E. S., “Nonlinear Lifting Line Theory for Predicting Stalling Instabilities on Wings of Moderate Aspect Ratio,” Tech. rep., General Dynamics Convair Report CASD-NSC-76-001, June 1976.
- ⁹Schairer, R. S., “Unsymmetrical Lift Distributions on a Stalled Monoplane Wing,” Thesis, California Institute of Technology, 1939.
- ¹⁰Sears, W. R., “Some Recent Developments in Airfoil Theory,” *Journal of The Aeronautical Sciences*, Vol. 23, May 1956, pp. 490–499.
- ¹¹Sivells, J. C. and Neely, R. H., “Method for Calculating Wing Characteristics by Lifting-Line Theory Using Nonlinear Section Lift Data,” NACA TN 1269, April 1947.
- ¹²Tani, I., “A Simple Method of Calculating the Induced Velocity of a Monoplane Wing,” Rep. No. 111 (vol. 9, 3), Aero. Res. Inst., Tokyo Imperial Univ., August 1934.
- ¹³M. Wickenheiser, A. and Garcia, E., “Extended Nonlinear Lifting-Line Method for Aerodynamic Modeling of Reconfigurable Aircraft,” *Journal of Aircraft*, Vol. 48, No. 5, September–October 2011, pp. 1812–1816.
- ¹⁴Gallay, S. and Laurendeau, E., “Nonlinear Generalized Lifting-Line Coupling Algorithms for Pre/Poststall Flows,” *AIAA Journal*, Vol. 53, No. 7, April 2015, pp. 1784–1792.
- ¹⁵Mukherjee, R. and Gopalathnam, A., “Poststall Prediction of Multiple-Lifting-Surface Configurations Using a Decambering Approach,” *Journal of Aircraft*, Vol. 43, No. 3, May–June 2006, pp. 660–668.
- ¹⁶Paul, R. C. and Gopalathnam, A., “Iteration Schemes for Rapid Post-Stall Aerodynamic Prediction of Wings Using a Decambering Approach,” *International Journal for Numerical Methods in Fluids*, July 2014.
- ¹⁷Hosangadi, P., Paul, R., and Gopalathnam, A., “Improved Stall Prediction for Swept Wings Using Low-Order Aerodynamics,” AIAA Paper 2015-3159, June 2015.
- ¹⁸Jamwal, A., *Computational Study of Aspect-Ratio Effects on Swept-Wing Stall*, Master’s thesis, North Carolina State University, Dec. 2017.
- ¹⁹Narsipur, S., *Low-Order Modeling of Dynamic Stall on Airfoils in Incompressible Flow*, Ph. D. Thesis, North Carolina State University, 2017.
- ²⁰Katz, J. and Plotkin, A., *Low-Speed Aerodynamics*, Cambridge Aerospace Series, 2000.
- ²¹Harper, C. W. and Maki, R. L., “A Review of the Stall Characteristics of Swept Wings,” NASA TN D-2373, 1964.
- ²²Silverstein, A., Katzoff, S., and Bullivant, W. K., “Downwash and Wake Behind Plain and Flapped Airfoils,” NACA Report No. 651, 1939.

²³Betz, A., “A Method for Direct Determination of Wing-Section Drag,” NACA TM-337, 1925.